Bio-Design and Manufacturing (2022) 5:277–293
https://doi.org/10.1007/s42242-021-00162-3

RESEARCH ARTICLE

Multiscale design and biomechanical evaluation of porous spinal fusion cage to realize specified mechanical properties

Hongwei Wang[1,2] · Yi Wan[1,2] · Quhao Li[1,2] · Xinyu Liu[3] · Mingzhi Yu[1,2] · Xiao Zhang[1,2] · Yan Xia[1,2] · Qidong Sun[1,2] · Zhanqiang Liu[1,2]

Received: 30 December 2020 / Accepted: 21 July 2021 / Published online: 24 November 2021

Abstract

Background Dense titanium (Ti) fusion cages have been commonly used in transforaminal lumbar interbody fusion. However, the stiffness mismatch between cages and adjacent bone endplates increases the risk of stress shielding and cage subsidence.

Methods The current study presents a multiscale optimization approach for porous Ti fusion cage development, including microscale topology optimization based on homogenization theory that obtains a unit cell with prescribed mechanical properties, and macroscale topology optimization that determines the layout of framework structure over the porous cage while maintaining the desired stiffness. The biomechanical performance of the designed porous cage is assessed using numerical simulations of fusion surgery. Selective laser melting is employed to assists with fabricating the designed porous structure and porous cage.

Results The simulations demonstrate that the designed porous cage increases the strain energy density of bone grafts and decreases the peak stress on bone endplates. The mechanical and morphological discrepancies between the as-designed and fabricated porous structures are also described.

Conclusion From the perspective of biomechanics, it is demonstrated that the designed porous cage contributes to reducing the risk of stress shielding and cage subsidence. The optimization of processing parameters and post-treatments are required to fabricate the designed porous cage. The present multiscale optimization approach can be extended to the development of cages with other shapes or materials and further types of orthopedic implants.

✉ Yi Wan
wanyi@sdu.edu.cn

[1] Key Laboratory of High Efficiency and Clean Manufacturing, School of Mechanical Engineering, Shandong University, Jinan 250061, China

[2] National Demonstration Center for Experimental Mechanical Engineering Education, School of Mechanical Engineering, Shandong University, Jinan 250061, China

[3] Department of Orthopedics, Qilu Hospital of Shandong University, Jinan 250012, China

Graphic abstract

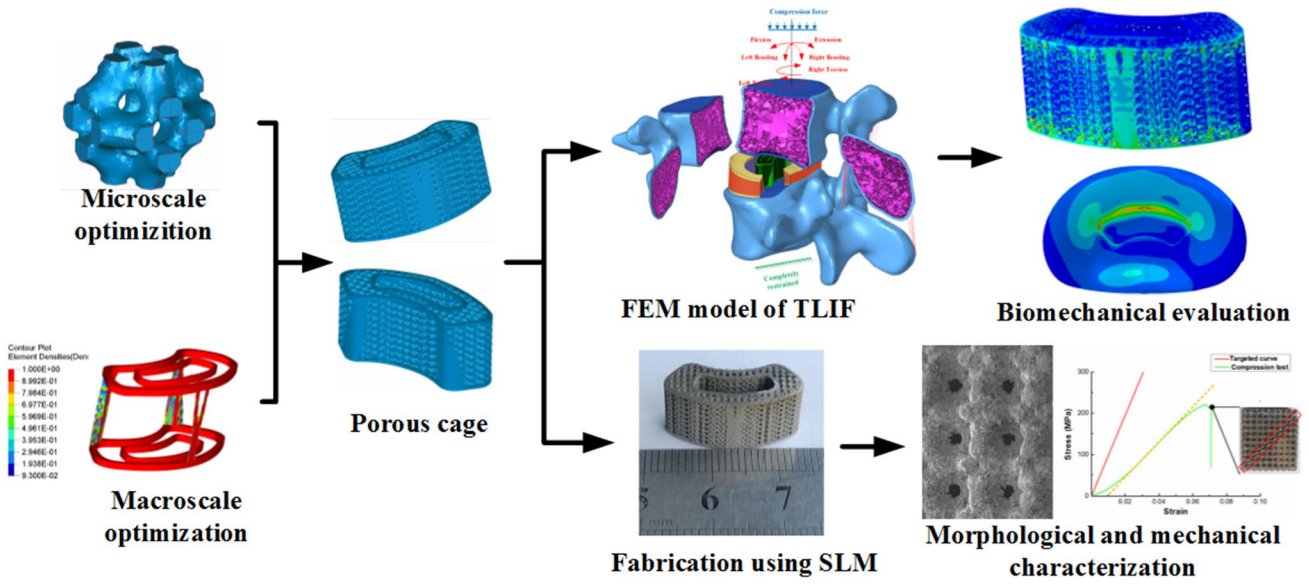

Keywords Topology optimization · Finite element method · Porous fusion cage · Lumbar spine · Selective laser melting

Introduction

Transforaminal lumbar interbody fusion (TLIF) is a commonly used surgical procedure to treat degenerative disc disease and spondylolisthesis when physiotherapy and medications fail to relieve the symptoms [1]. The implanted fusion cage restores the immediate intervertebral height and supports the anterior weight of the vertebrae, while bone grafts surrounding the cage fuse with adjacent vertebrae over time following TLIF. Conventional titanium (Ti) fusion cages exhibit satisfactory biocompatibility, corrosion resistance, and mechanical strength [2]. However, the stiffness mismatch between cages and adjacent bone endplates increases the risk of stress shielding and cage subsidence [3, 4]. The rigid Ti cage shields the implanted bone grafts from the necessary mechanical stimuli, thus impeding bone remodeling and its fusion with the adjacent bone endplates according to Wolff's law. Clinical studies have demonstrated that low-stiffness cages exhibit better fusion performance versus dense Ti cages [5, 6]. In addition, cage subsidence has been reported to be linked to the increased stress on bone endplates caused by the high stiffness of Ti cages [7–9]. Alternatively, dense polyetheretherketone cages with an elastic modulus that is more similar to bone endplates have been used in TLIF to reduce the risk of stress shielding and cage subsidence. However, the inherent poor osseointegration of polyetheretherketone is unfavorable for achieving fusion and long-term stability [1, 10]. In recent decades, multiple strategies have been developed to reduce the stiffness of Ti cages for improved fusion performance.

Porous Ti cages have been proposed as promising candidates due to the option to adjust their stiffness by tailoring the geometrical parameters of pore structure. Moreover, the porous structure provides channels for bone ingrowth to avoid cage dislocation. Recent advances of additive manufacturing techniques, especially metallic powder bed-based ones, such as selective laser melting (SLM) and electron beam melting, enable the production of load-bearing porous implants [11, 12]. Numerical and experimental studies have demonstrated that the biomechanical performance of porous cages is satisfactory and superior to dense cages [13, 14]. In vivo experiments have also illustrated the adequate fusion performance of various porous Ti cages [15–17]. The overall stiffness of cages decreases with the increase in porosity and is also associated with the topological feature of unit cells [18]. Variations in the topology of unit cells affect their mechanical performance, which further influences the macroscopic mechanical performance of porous implants [19]. The porous structure design has been of particular interest due to its significant association with the biomechanical performance of implants.

Various methodologies have been proposed for porous implant development, including the computer-aided design (CAD) method, implicit-based method, or topology optimization [20, 21]. The latter is a mathematical approach seeking optimal material distribution with the desired mechanical properties under specified loading conditions. Porous implants consist of basic unit cells, whose mechanical

properties play a critical role in the overall mechanical performance of porous implants. Recent studies have focused on optimizing the basic unit cells to achieve a satisfactory mechanical performance of porous implants [22–26]. Xiao et al. [25] obtained isotropic unit cells with the maximum acquirable stiffness under constraints of volume fractions. Yang et al. [26] developed a method for designing unit cells with prescribed mechanical properties based on the homogenization theory. Guest et al. [27] proposed a microstructure design with maximized stiffness and fluid permeability using topology optimization. Meanwhile, the global structural design of the porous structure is not considered in these studies. In order to enhance the overall biomechanical performance of porous implants, multiscale optimization methods emerged, including unit cell optimization and global structure optimization. In Moussa's study [28], topology optimization was utilized to determine different unit cell distributions in a cervical porous cage. The developed porous cage contributed to reducing the risk of cage subsidence; however, its biomechanical performance was not evaluated comprehensively. In Wang's study [29], a reinforced porous cage consisting of a porous structure and frameworks, designed using a multiscale optimization approach, exhibited satisfactory biomechanical performance. The framework constructed on the porous cage reduced the peak stress on the cage but increased its overall stiffness. The biomechanical performance of the cage might be further improved by the elimination of stiffness difference between the bone endplates and the reinforced porous cage.

Inspired by previous studies [26, 29], microscale optimization based on the homogenization theory can be used to acquire the unit cell with the specified mechanical properties; constructing frameworks on the porous cage while reducing its negative effects on the overall stiffness might enhance the biomechanical performance of the porous cage. The present study proposes a multiscale optimization approach for porous cage development to eliminate the stiffness difference between the implant cage and the adjacent bone endplates. A finite element method (FEM) model of TLIF was developed to assess the biomechanical performance of the optimized porous cage under physiological loading conditions. The designed porous cage was fabricated via SLM to assess the morphological and mechanical difference between as-designed and fabricated samples.

Materials and methods

Optimization of porous cage

The multiscale optimization approach focuses on developing a porous fusion cage with equivalent stiffness to match that of bone endplates under physiological loading conditions, including microscale optimization seeking an optimal unit cell with prescribed mechanical properties and macroscale optimization determining the layout of framework structure over the porous cage.

Microscale optimization

It is assumed that the size of unit cells is much smaller than the cage geometry. Hence, the homogenization theory enables the estimation of effective elasticity properties of porous structures that are periodically assembled by unit cells. The effective elasticity tensor is expressed in energy form as

$$D^H_{ijkl} = \frac{1}{|Y|}\int_Y \left(\varepsilon^{0(ij)}_{pq} - \varepsilon^{(ij)}_{pq}\right)^{\mathrm{T}} D_{pqrs}(\rho_e)\left(\varepsilon^{0(kl)}_{rs} - \varepsilon^{(kl)}_{rs}\right)\mathrm{d}Y \quad (i,j,k,l = 1,2,3) \tag{1}$$

where Y denotes the volume of unit cell domain Y, $\mathrm{D}_{pqrs}(\rho_e)$ denotes the elemental elasticity tensor, $\varepsilon^{0(kl)}_{\mathrm{pq}}$ denotes the initial unit strain matrix, and $\varepsilon^{(ij)}_{pq}$ is defined as

$$\varepsilon^{(ij)}_{pq} = \varepsilon_{pq}\left(\chi^{ij}\right) = \frac{1}{2}\left(\chi^{ij}_{p,q} + \chi^{ij}_{q,p}\right) \tag{2}$$

based on the displacement field χ^{kl} found by solving the elasticity equations:

$$\int_Y D_{jipq}(\rho_e)\varepsilon_{ij}(y)\varepsilon_{pq}\left(\chi^{kl}\right)\mathrm{d}Y = \int_Y D_{jipq}(\rho_e)\varepsilon_{ij}(y)\varepsilon^{0(kl)}_{pq}\mathrm{d}Y, \quad \forall y \in Y \tag{3}$$

where y is a virtual displacement field. The detailed description of homogenization can be found in the literature [30–32].

To avoid the intermediate values, $D(\rho_e)$ is interpolated using the solid isotropic material with penalization (SIMP) method as follows:

$$D(\rho_e) = \rho_e^p D_0, \tag{4}$$

where D_0 denotes the elasticity tensor for solid element, $p = 3$ denotes the exponent of penalization, and ρ_e denotes the relative density of element.

A unit cell with stiffness lower than that of bone endplates contributes to reducing the effect of framework structure on the overall stiffness of the porous cage. In order to achieve optimal overall stiffness and maximize the volume for bone ingrowth at the same time, microscale optimization is used to maximize the porosity of unit cell subject to the equivalent stiffness to 80% elastic modulus of bone endplates. To make the objective function more achievable, the bone endplate is simplified into an isotropic elastic material (Table 1) in the inverse homogenization process.

Table 1 Material properties used in optimization and TLIF model

Component	Elastic modulus (MPa)	Poisson ratio
Bone endplate	12,000	0.3
Titanium	110,000	0.3
Bone grafts	100	0.2

The base material Ti is assumed to be an isotropic material with linear elastic properties (Table 1). A function is formulated in terms of the discrepancy between the corresponding entries of the targeted elasticity tensor and the calculated effective elasticity tensor. The mathematical description of the microscale topology optimization is as follows:

$$\text{Objective function}: \text{Minimize}\ (V_{\text{micro}} = \sum_{e} \rho_e V_e) \tag{5}$$

$$\text{Subject to}: \ 0 < \rho_{\min} \le \rho_e \le 1 \tag{6}$$

$$\sum_{i,j,k,l}^{3} \left(D^{*}_{ijkl} - D^{H}_{ijkl}(\rho_e) \right)^2 = 0 \tag{7}$$

where V_{micro} denotes the computed volume of unit cell, V_{e} denotes the volume of element (e), $\rho_{\min} = 0.001$ is used to avoid the singularity of the global stiffness matrix, and D^{*}_{ijkl} denotes the targeted elasticity tensor.

Considering the manufacturing constraints and appropriate pore sizes for bone ingrowth [28, 33], a cube with a size of 1 mm × 1 mm × 1 mm is set as the basic cell of microscale optimization and meshed using 20 × 20 × 20 eight-node cubic elements. Sensitivity filters are adopted to avoid the checkerboard pattern, and the method of moving asymptotes [34] is adopted to update the density design variables. A MATLAB code is developed to achieve optimization. Figure 1 depicts the workflow of microscale topology optimization for unit cell development.

In order to enhance the fatigue resistance of the porous structure, the optimized unit cell is smoothed with the main topology feature reserved and converted to the STL files. Next, the STL file is imported into Solidworks (Dassault Systemes SolidWorks Corp., USA) and used to construct the corresponding porous structure by periodically repeating the unit cell along all directions. A numerical homogenization conducted by Comsol software calculates the effective elasticity tensor of the smoothed unit cell. A porous structure of 10 × 10 × 10 unit cells is used in the numerical simulation of compression test to attain the stress–strain curve of the porous structure.

Macroscale optimization

The structure with stiffness equivalent to the bone endplates under specified physiological loading conditions can be achieved via the constraints of displacements under specified loading conditions. To acquire the displacement constraints used for optimization, this study uses Altair Hypermesh (Altair Engineering Inc., USA) to develop a FEM model of a traditional dense crescent cage, which

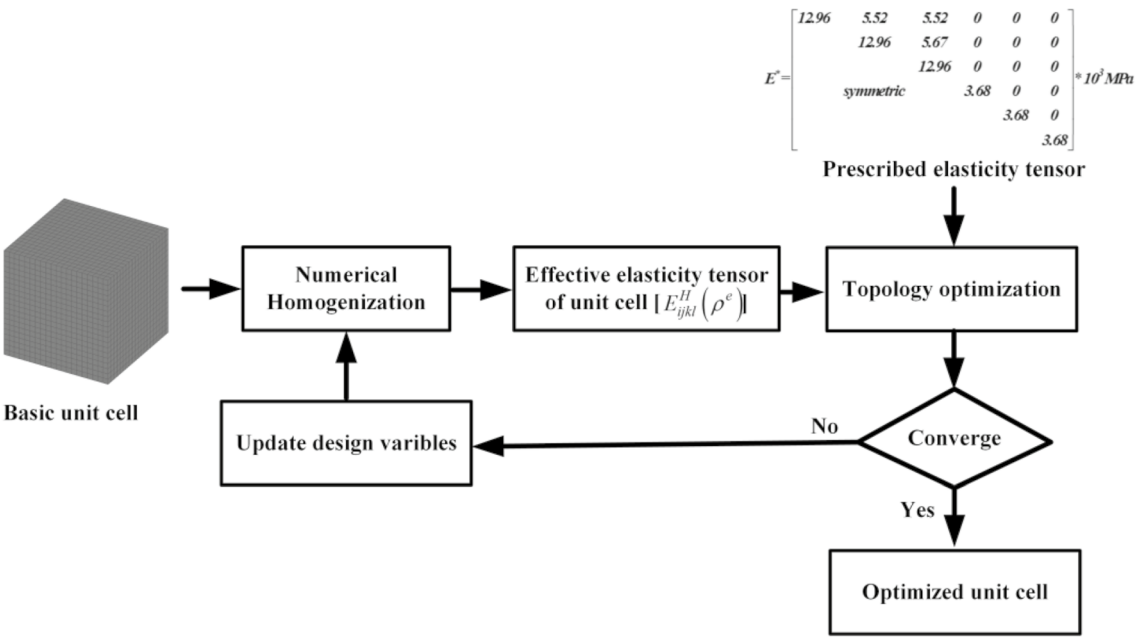

Fig. 1 Flowchart of microscale topology optimization

adopts the mechanical properties of bone endplates with the inferior surface fully restrained and the superior surface rigidly connected to a master node (Fig. 2). The superior and inferior surface profiles of the cage conform to the adjacent bone endplates. To achieve an appropriate overall stiffness of the porous cage, the displacements of the master node are obtained by imposing physiological loading conditions, including 10 N·m flexion, extension, and bending on the master node. The objective of global optimization is to minimize the volume of solid portions that are subject to stiffness constraints. The mathematical formulation of the macroscale topology optimization problem is the following:

$$\text{Objective function: Minimize} \left(V_{\text{macro}} = \sum_j x_j V_j \right) \tag{8}$$

$$\text{Subject to}: \ 0 < x_{\min} < x_j < 1 \quad (j = 1, 2, 3, \ldots, n) \tag{9}$$

$$U_k \le \overline{U}_k \tag{10}$$

where V_{macro} denotes the computed volume of global structure, x_j denotes the density variables that are assigned to each element (j), $x_{\min} = 0.001$ denotes the specified minimum density, V_j denotes the element volume (j), U_k denotes the computed displacements of the master node (k), and $\overline{U}_k$ denotes the specified displacement of the master node (k).

The elasticity matrix E is expressed as the interpolation function as follows:

$$E = x_j^p \left(E_1 - E_2 \right) + E_2, \tag{11}$$

where $p = 3$ denotes the exponent of penalization, E_1 denotes the elasticity tensor of Ti, and E_2 denotes the elasticity tensor of the smoothed unit cell.

Macroscale optimization is conducted using Altair OptiStruct (Altair Engineering Inc., USA). In order to enhance the load transmission, the dense Ti structure as a framework structure is added along the superior and inferior edge of the cage (Fig. 2) [35]. The outer portion in the middle of the cage is set as the design domain.

The final framework structure consists of the reserved portion of the design domain after optimization and the predefined framework structure in the non-design domain. A Boolean intersection operation between the dense cage and the porous structure generates the initial porous cage. Subsequently, a Boolean union operation between the framework

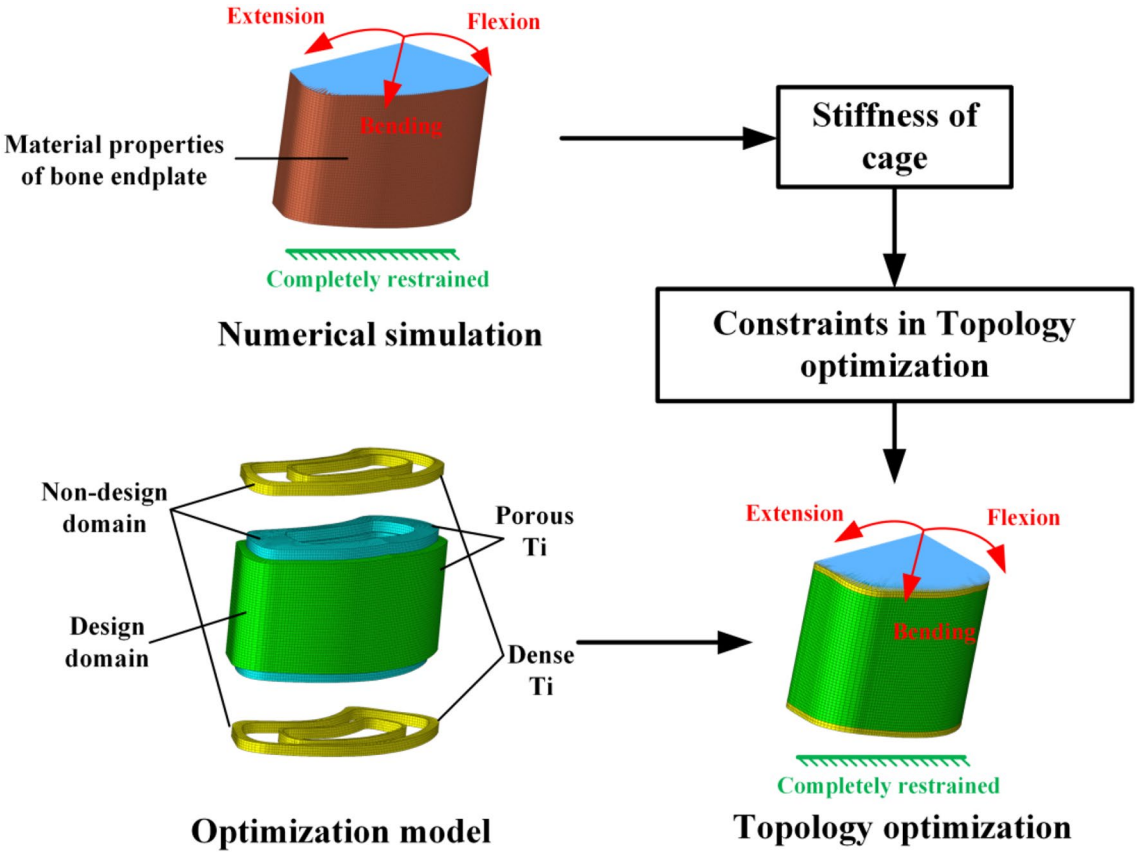

Fig. 2 Macroscale topology optimization of porous cage

structure and the initial porous cage generates the final porous cage. To verify the stiffness of the final porous cage, numerical simulations of the porous cage are conducted to obtain the displacements of the specified node under 10 N·m flexion, extension, and bending load conditions.

Biomechanical analysis of cage in TLIF

The partial annulus fibrosus and nucleus pulposus are removed from the validated FEM model of the lumbar spine L4-L5 segment [36], thus generating the FEM model of TLIF. The porous fusion cage is meshed using tetrahedron elements with 0.1 mm length to accurately demonstrate stress distributions on it. The bone endplates and cancellous bones neighboring the fusion cage are refined using typical elements with 0.1 mm length, resulting in approximately 5.5 million elements for the porous cage model (Fig. 3a). A dense Ti cage with an identical global shape is included for biomechanical assessment. It is meshed using tetrahedron elements with 0.2 mm lengths, resulting in approximately 3.4 million elements for the dense cage model. All interfaces between endplates and cages are assumed as frictional contacts with a friction coefficient of 0.8 [37]. The inferior bone endplate of the L5 vertebrae is completely restrained. A 400 N following compressive load is applied perpendicular to the superior bone endplate of L4 vertebrae, and 10 N·m moments are loaded to simulate flexion, extension, left bending, right bending, left torsion, and right torsion load conditions, respectively [38, 39]. Mesh convergence is performed based on the stress values on the cage and bone endplates, which verify the element sizes for sufficient accuracy.

To date, there is no direct index for cage subsidence. It is extensively accepted that the high stress on bone endplate is one of its primary causes [8, 28]. In the present study, the high stress is taken as an indicator for cage subsidence. In addition, the detailed architecture of the porous fusion cage increases the difficulty of meshing bone grafts. A solid-mimic porous cage is developed with the porous portion adopting the effective elasticity tensor of the smoothed unit cell and the framework adopting the mechanical properties of Ti. The strain energy density (SED) of bone grafts, which has been widely accepted as an index of mechanical stimulus for bone remodeling, is quantified to perform the risk assessment of stress shielding (Fig. 3b) [40–42]. The bone grafts (from local morselized bone) are simplified as a linear elastic material (Table 1) and densely filled in the remaining space surrounding the cage [43, 44]. Frictionless contact is assumed at the interface between bone grafts and adjacent tissue, bone grafts and cage, to simulate the initial postoperative

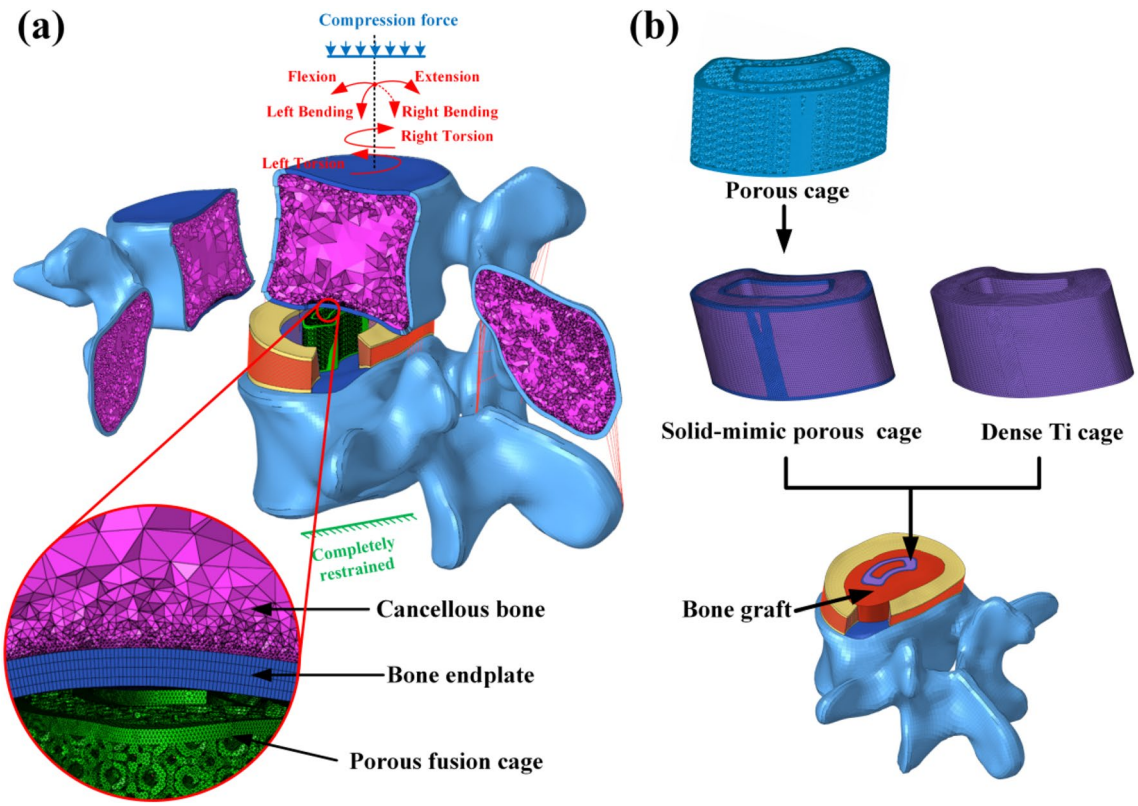

Fig. 3 **a** FEM model of TLIF; **b** the implanted cage and bone grafts in the TLIF model

period. The stiffness of the solid-mimic cage under flexion, extension, and bending is assessed for the validation. In addition, stresses at identical positions of the framework structure in the porous cage and the solid-mimic porous cage are quantified to assess the mechanical differences of the framework in cages under different loading conditions. All simulations are conducted using Abaqus software (Dassault Systems Simulia Corp., USA).

Fabrication and characterization

The porous structure and the final porous cage are fabricated using a Prox DMP 320 machine (3D Systems, Belgium). Commercially available Ti-6Al-4 V powder with an average diameter of 40 μm is selected as starting material with processing parameters shown in Table 2. The fabricated porous structure and cages are removed from the substrate plate using electrical discharge machining and are ultrasonically cleaned in acetone, anhydrous ethanol, and distilled water for 15 min. Furthermore, heat treatment is performed at 800 °C for 4 h in a vacuum environment to eliminate the residual thermal stress.

The morphology of porous structure is observed by scanning electron microscopy (JSM-7610F, JEOL, Tokyo, Japan). The fabricated porous structure is polished using the standard metallographic procedure to observe its microstructure. To assess the compressive performance of the fabricated porous structure, a uniaxial compression test is carried out using an ME50 universal mechanical testing machine (Senkeino Technology co. Ltd., China) according to ISO 13314:2011. The maximum testing force is 50 KN, and the test force error is < 0.5%. Three samples are compressed at a constant cross-head speed of 1 mm/min. The elastic modulus of the fabricated porous structure is calculated based on the slope of stress–strain curves within the linear deformation region, and the yield strength of the porous structure is defined as the 2% offset line. The elastic modulus of the porous structure is analyzed using GraphPad Prism 6.0 software (GraphPad Software Inc., USA), and a value of $p < 0.05$ is set to indicate statistical significance.

Table 2 Processing parameters of SLM

Parameter	Value
Laser power	145 W
Laser spot size	60 μm
Mark speed	1000 mm/s
Hatch distance	78 μm
Layer thickness	30 μm
Oxygen content	< 0.1 wt%

Results

Optimization results

Microscale optimization yields an optimized unit cell, as shown in Fig. 4. Smoothed surface morphology is observed on the final unit cell after smoothing with the main topological feature reserved. The porosity of the porous structure is 72.2%, and the sizes of three different pores in the unit cell are approximately 400, 200, and 200 μm, respectively. The elastic module of the porous structure is approximately 9470 MPa, which is calculated based on the slope of the stress–strain curve before the strain approaches 0.1. The effective elasticity tensor of the unit cell calculated by numerical homogenization corresponds well to the compression simulation. The elastic modulus and Poisson ratio derived from effective elasticity tensor are approximately 9830 MPa and 0.3, respectively. As the Poisson ratio cannot be obtained through compression simulation, the effective elasticity matrix is adopted as E_2 in the macroscale optimization. The macroscale optimization result illustrates the layout of the framework structure in the porous cage, which contains partial materials with a relative density lower than 1 for smoothing the surface of the framework structure. The final porous cage generated by the Boolean union operation between the initial porous cage and the framework structure is shown in Fig. 4. The displacements of the specified node under flexion, extension, and bending load conditions are listed in Fig. 5 to evaluate the stiffness of the porous cage. The displacements, which are slightly lower than the targeted values under flexion, extension, and bending, indicate the slightly higher stiffness of the porous cage respective to the predicted values. In addition, the solid-mimic porous cage exhibits a stiffness equivalent to that of the porous cage.

Biomechanical performance of cages

As shown in Fig. 6, stress distribution on both the dense cage and the porous cage is associated with loading conditions. A similar distribution but a different peak stress value is observed between the dense cage and the porous cage under all loading conditions. In comparison with the dense cage, the peak stress on the porous cage is increased by 178%, 98%, 130%, 180%, 153%, and 233% under flexion, extension, left bending, right bending, left torsion, and right torsion, respectively. The peak stress concentrates on the minor diameter or the thin-walled regions of the porous structure. The stress distribution on the solid-mimic porous cage is demonstrated in Fig. 6. Differences in the peak stress value and distribution are detected

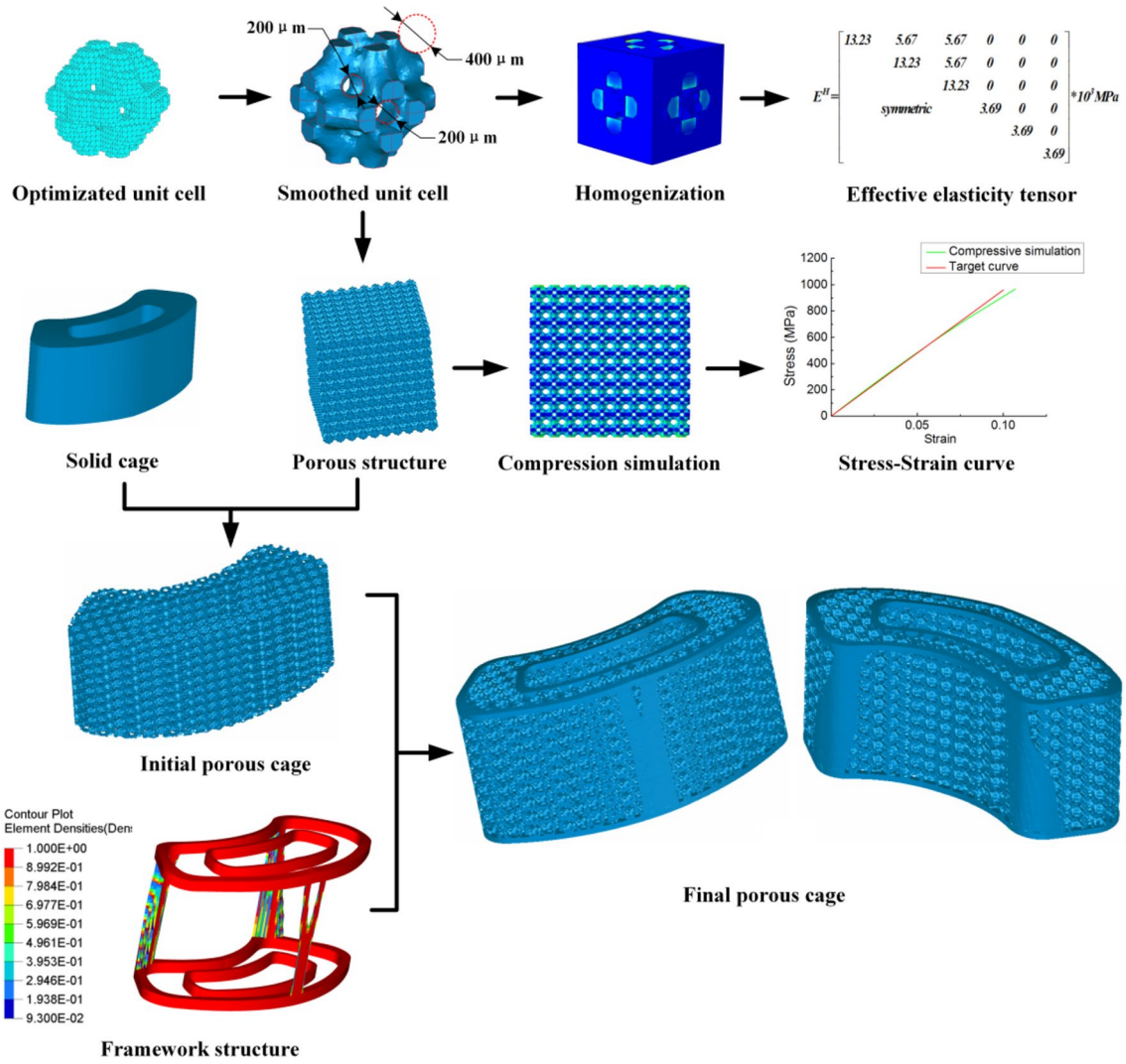

Fig. 4 Multiscale optimization result

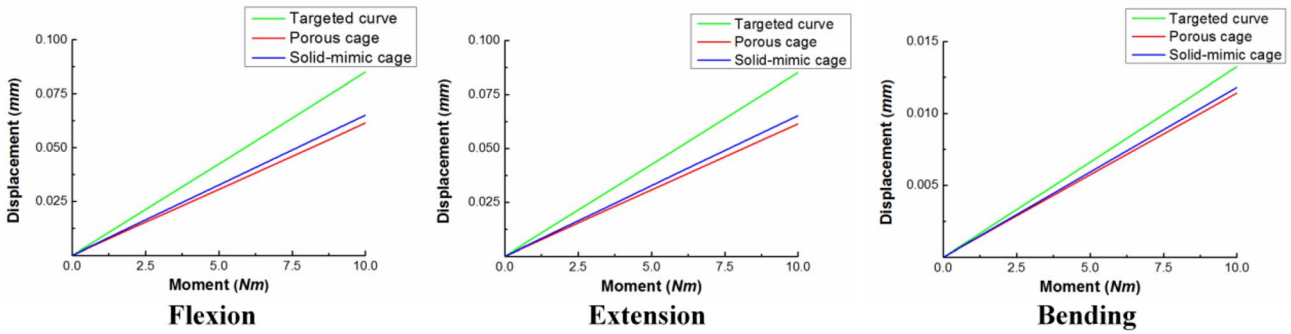

Fig. 5 The displacement–moment curve of the specified node under different loading conditions

between the porous cage and the solid-mimic porous cage. The peak stress is located at the framework of the solid-mimic porous cage under all loading conditions. The peak stress values on the portion mimicking the porous structure are 76, 115, 104, 106, 44, and 47 MPa under flexion, extension, left bending, right bending, left torsion, and

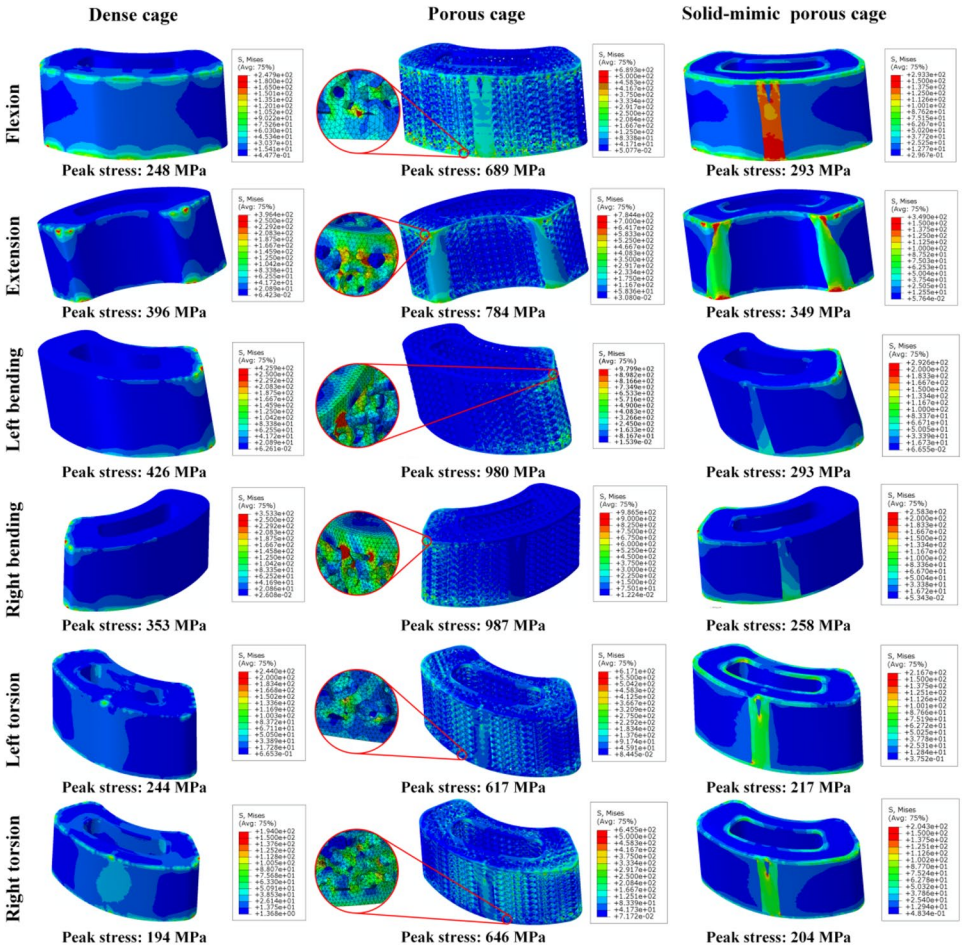

Fig. 6 Stress distribution on cages under physiological loading conditions

right torsion, respectively. As shown in Fig. 7, slight differences of stress values on the identical nodes of frameworks are observed between the porous cage and the solid-mimic porous cage. The solid-mimic porous cage enables the description of the stress distribution on the porous cage frameworks, but is not capable of demonstrating the stress on the porous structure of the porous cage.

As shown in Figs. 8 and 9, the location of peak stress concentration on bone endplates is correlated with loading conditions. The peak stress on both the superior and inferior bone endplates is located at the contact interface with fusion cage edges. A similar distribution but different peak values are observed between the dense cage and porous cage models. The values of peak stress on the superior bone endplate of the porous cage model are reduced by 11.9%, 12.7%, 9.1%, 8.4%, 11%, and 2.6% versus the dense cage model under flexion, extension, left bending, right bending, left torsion, and right torsion, respectively. The values of peak stress on the inferior bone endplate of the porous cage model are reduced by 13.2%, 9.6%, 10.4%, 10.5%, 7.8%, and 15.4%, respectively, as compared with the dense cage model. From a biomechanical viewpoint, the porous cage with lower stiffness contributes to reducing the risk of cage subsidence under all loading conditions. In addition, a similar distribution but different peak values are also observed between the porous cage and solid-mimic porous cage models, which may be due to the slight difference in stiffness between the two cages under all loading conditions.

Compared with the dense cage model, the SED of bone grafts in the solid-mimic porous cage model is increased by 7%, 4%, 7%, 6%, 3%, and 4%, under flexion, extension, left bending, right bending, left torsion, and right torsion, respectively (Fig. 10). Therefore, more load is transmitted through the bone grafts in the solid-mimic porous cage model under physiological loading conditions. The designed porous cage contributes to alleviating the stress shielding effect of the cage during the initial postoperative period.

Structural and mechanical characterization of fabricated samples

The unit cell fabricated via SLM is shown in Figs. 11a and 11b. When observing the main topological feature, a surface morphological deviation is detected between the as-designed and the fabricated unit cell. Unmelted Ti

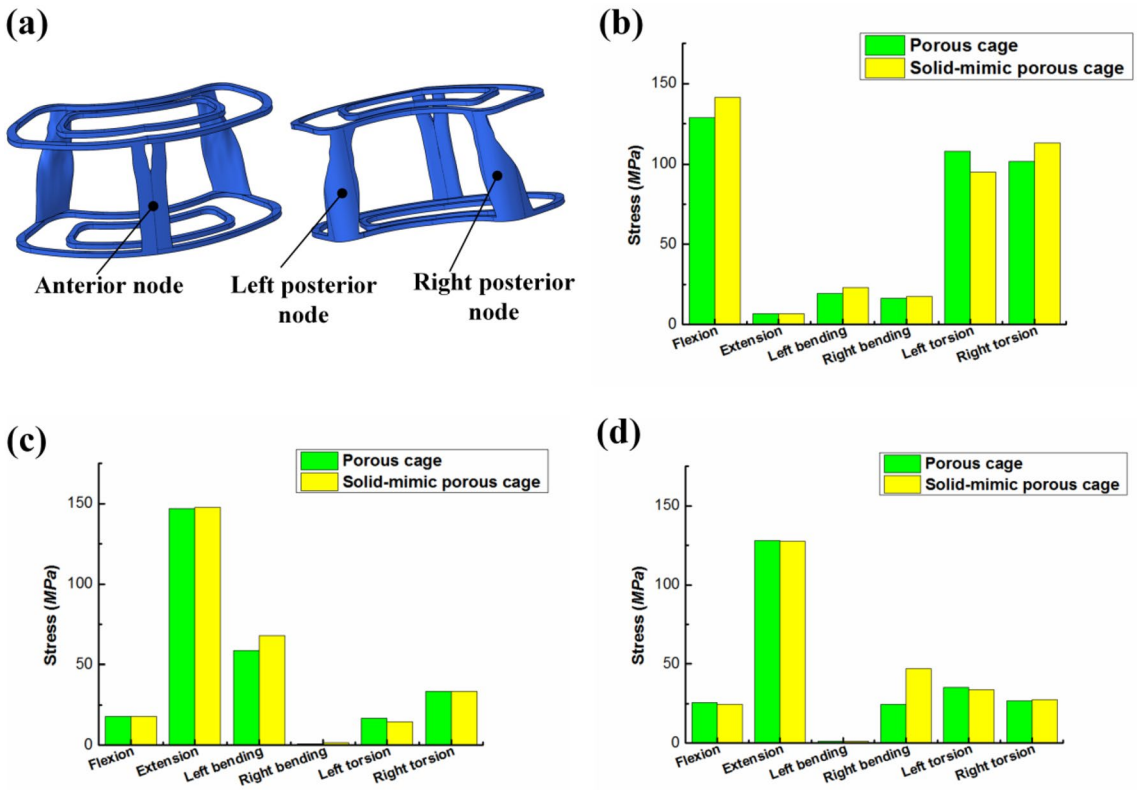

Fig. 7 **a** Selected nodes on the framework structure of cages. The stress on **b** anterior nodes, **c** left posterior nodes, and **d** right posterior nodes

particles are adhered to the surface of the unit cell, thus lowering the surface quality. The pores with 400 μm size are reserved (Fig. 11c). However, a portion of the other two pores with 200 μm size are blocked by the unmelted Ti particles despite the ultrasonic cleaning step. Moreover, imperfections such as residual pores and cracks are detected on the fabricated sample (Fig. 11d). Figure 11e shows the fabricated porous structure used for the compression test. The fabricated porous cage is presented in Figs. 11f and 11g, where the porous structure and frameworks can be distinguished.

The mean curve and standard deviations of the stress–strain curves are shown in Fig. 11h. The fabricated porous structure possesses a linear elastic deformation stage before the strain reaches 0.06, followed by a fracture along an oblique direction of 45 degrees (Fig. 11h). No obvious plastic deformation or densification stages are observed. The elastic modulus of fabricated porous structure is 4.1 ± 0.1 GPa, and the yield strength of porous structure is 209 ± 7.6 MPa. A significant difference ($p < 0.05$) is observed between the elastic modulus of the fabricated porous structure and that calculated by numerical homogenization.

Discussion

In this study, the unit cell with prescribed mechanical properties, which is lower than bone endplates, is obtained via microscale topology optimization. For better fatigue resistance, smoothing is conducted on the unit cell while reserving the main topological feature [45]. Both the stress–strain curve obtained via uniaxial compression simulation and the effective elasticity tensor calculated by numerical homogenization in Comsol software verify the elastic properties of the smoothed unit cell. All three types of pores present in the designed unit cell are within the favorable range for bone regeneration, whereas the optimum pore size remains controversial [46–49]. To achieve the prescribed overall stiffness of the cage, no morphological or dimensional adjustment of the optimized framework structure is conducted after macroscale optimization. The final porous cage, obtained from the Boolean union operation between the porous structure and frameworks, exhibits a similar stiffness to bone endplates under physiological loading conditions. Moreover, the framework structure around the porous structure contributes to the reduction of

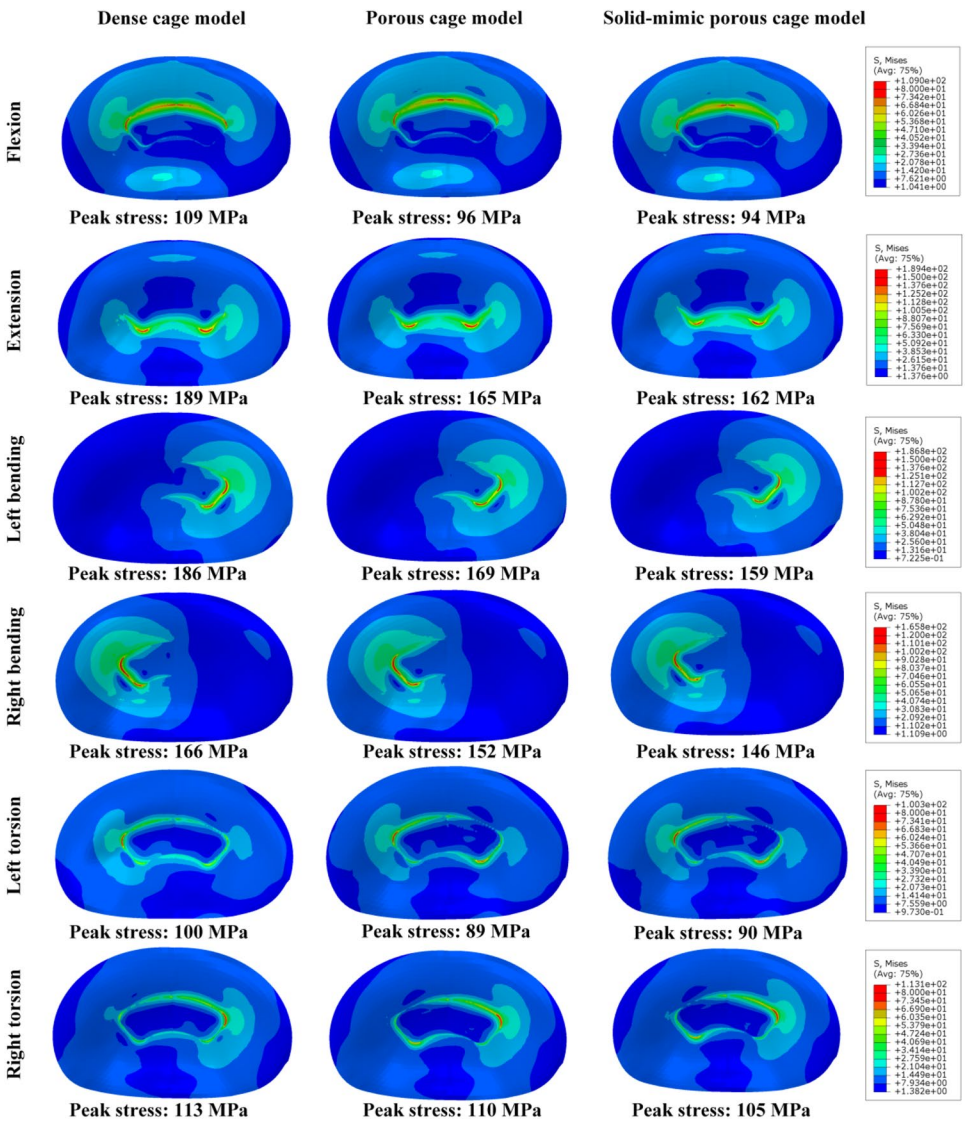

Fig. 8 Stress distribution on the superior bone endplate

peak stress on the porous cage, while the reserved majority of pores in the porous cage benefit bone ingrowth.

The region of high stress concentration on the porous cage under physiological loading conditions is in the high risk of fracture. The detailed meshed porous cage is used to illustrate the stress distribution in the cage. Despite the addition of the framework, the peak stress on the porous cage is higher than that on the dense cage under all loading conditions. The peak stress concentrates on the thin-walled structures of porous cage. In order to reduce the value of peak stress on porous cages, it is necessary to avoid the generation of thin-walled structure in the porous cage design, and posterior pedicle screw fixation is essential. According to the stress distribution on the framework structure of the porous cage and the solid-mimic porous cage, the solid-mimic porous implant is valid for the forecast of stress distribution on the frameworks, but is invalid for the porous structure. In addition, the stress on the solid portion mimicking the porous structure is dramatically lower than the yield strength derived by the compression test of the fabricated sample, though the imperfection in the fabricated porous structure tends to decrease the yield strength. However, local stress concentrations appearing at the minor diameter or thin-walled locations might lead to local collapse before the entire porous structure yields. The detailed mesh is essential for predicting the peak stress distribution on the porous cage.

The value of peak stress on both the superior and inferior bone endplates of the porous cage model decreases versus the dense cage model under physiological loading conditions, which is in accordance with previous studies [14, 28, 50]. The results indicate that the designed porous cage contributes to reducing the risk of cage subsidence. In addition, peak stress concentrates on the contact interface with the outer edge of cages under physiological loading conditions, which is in good agreement with a previous study [51]. The

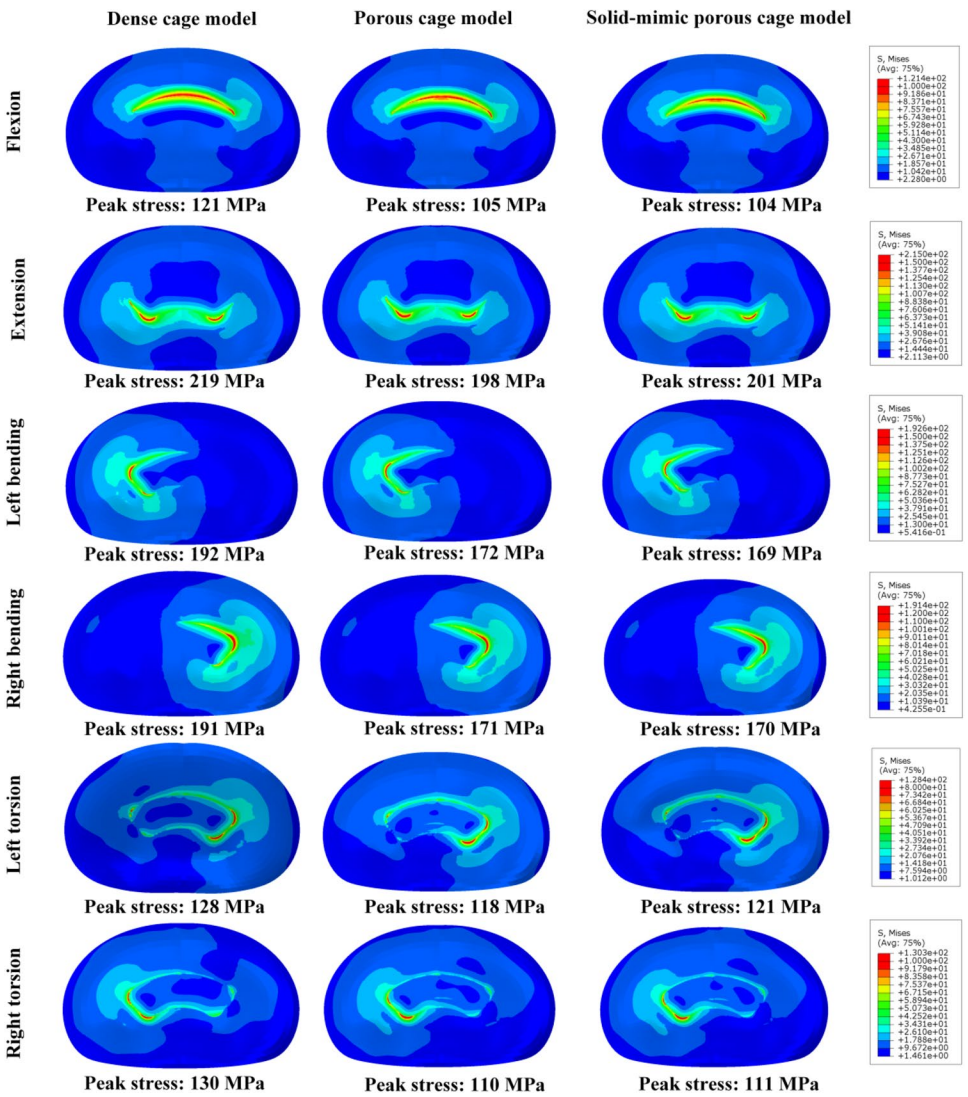

Fig. 9 Stress distribution on the inferior bone endplate

yield strength of bone endplate is approximately 173 MPa [43]. Extension and bending activity should be avoided in the initial postoperative period to reduce the risk of cage subsidence, and posterior pedicle screw fixation is recommended for fusion surgery to reduce peak stress on bone endplates. A clinical study conducted by Cabraja et al. [52] demonstrated that cage subsidence is associated with various factors, including the mechanical properties, shape, and surface architecture of cages. Arc edges as an alternative to sharp edges might further reduce the peak stress on bone endplates.

Porous structures mimicking dense material have been accepted for predicting the biomechanical effect of porous implants on adjacent tissues [50, 53]. Due to the identical stiffness to the porous cage under identical loading conditions, the solid-mimic cage is used to assess the SED of bone grafts. Under all simulated physiological loading conditions, the increased SED of bone grafts in the solid-mimic porous cage model indicates the reduced risk of stress shielding of the porous cage. Porous cages with reduced stiffness can reduce the risk of stress shielding and stimulate the bony fusion of bone grafts [29, 40]. From a biomechanical viewpoint, the porous cage proposed in this study contributes to enhancing the fusion of bone grafts in the initial postoperative period. However, the increased SED is not too noticeable likely because the stiffness of the porous cage is still high. An additional reduction of cage stiffness might further reduce the stress shielding effects.

The morphological and mechanical characterization of the fabricated porous structure is performed to assess the differences between the as-designed and fabricated porous structures. Although ultrasonic cleaning partially removes residual particles in the porous structure, Ti particles attached to the surface of unit cells conceal the designed morphology of the unit cell and decrease the size of pores. Some pores with 200 μm size are blocked by the particles

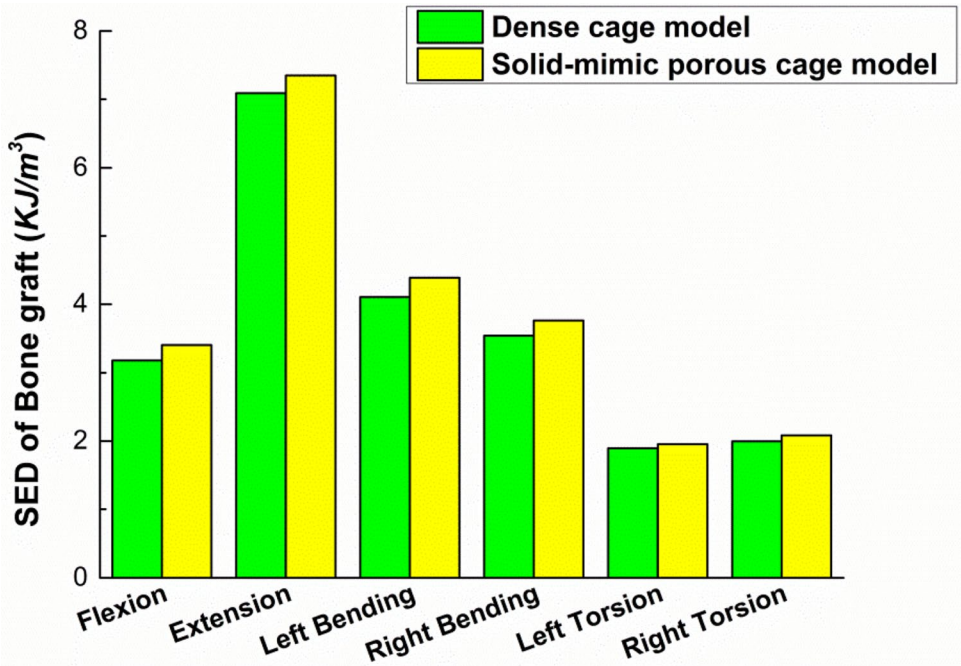

Fig. 10 SED of bone grafts under physiological loading conditions

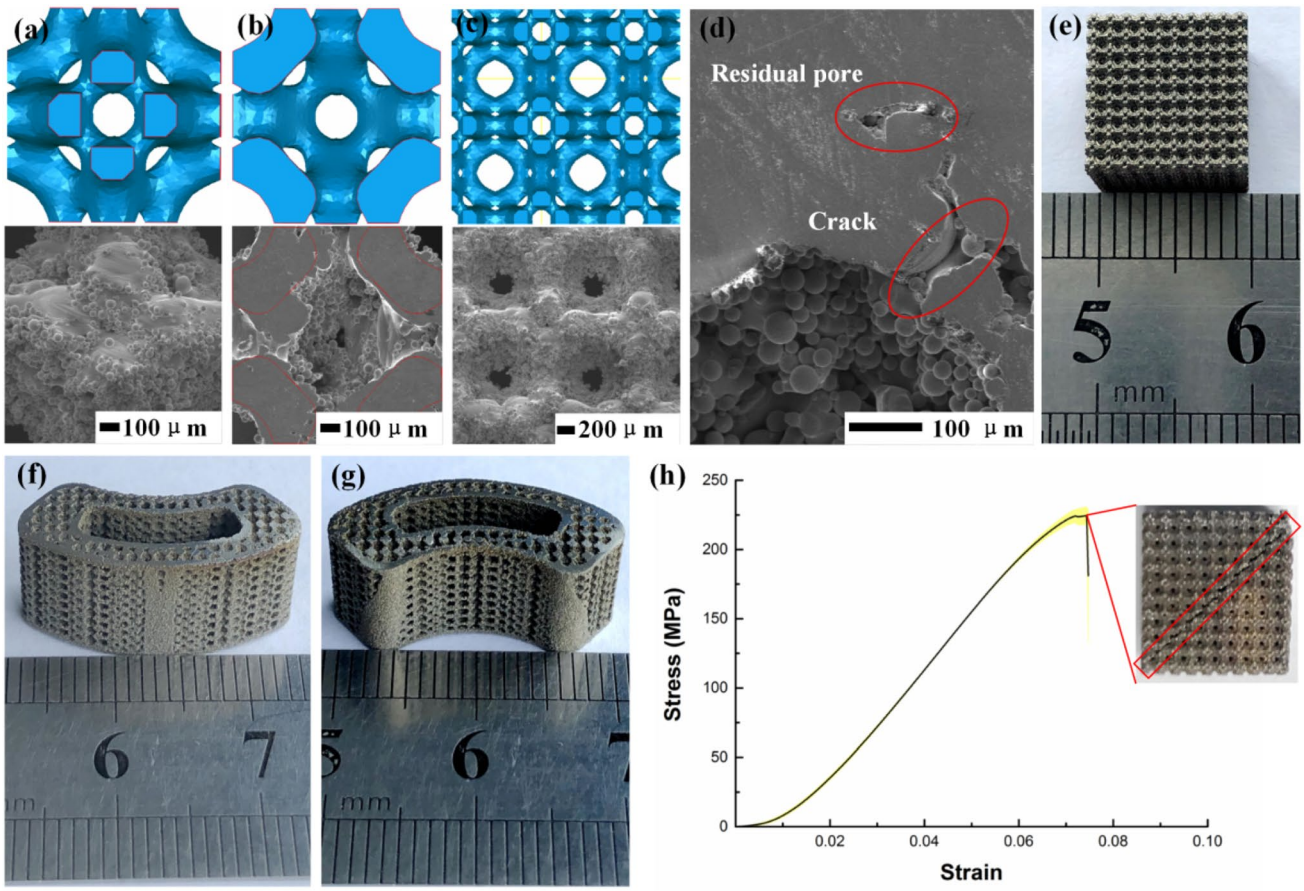

Fig. 11 **a** Morphological comparison of the as-designed and fabricated unit cell; **b** the sectional view of the as-designed and fabricated unit cell; **c** the as-designed and fabricated porous structure; **d** the imperfection on the microstructure; **e** the photographs of the fabricated porous structure used for the compression test; **f** the front top view of the fabricated porous cage; **g** the rear top view of the fabricated porous cage; **h** the compressive stress–strain curves of the fabricated porous structure

and further prevent internal loose particles from flowing out during ultrasonic cleaning. Moreover, unmelted particles may fall off from the surface and increase the risk of inflammation after implantation [54]. Post-treatments, such as acid etching, are essential to remove the residual particles. In addition, the compression test illustrates that the fabricated porous structure exhibits lower elastic properties than the as-designed porous structure. The mechanical properties of the designed cage used the FEM model are overestimated using the present SLM processing parameters. The mechanical properties of the fabricated structure are correlated with various factors, including processing parameters such as laser power, mark speed, and the inherent imperfection emerging from SLM resulting in residual pore and cracks (Fig. 11d) [55, 56]. Post-treatments such as heat treatment or hot isostatic pressing enable the mechanical performance improvement of the fabricated porous structure [55]. To attain the successful clinical application of the designed porous cage, further studies regarding the optimization of fabricating parameters and post-treatments are needed to alleviate the inherent imperfection of SLM, to obtain the as-designed surface morphology, and to improve the mechanical performance simultaneously.

Herein, the objective of microscale optimization is the acquisition of unit cell with an elastic modulus that is 20% lower than that of bone endplates. Unit cells with other values of elastic modulus that are lower than that of bone endplates can also be obtained in microscale optimization by varying the objective elasticity tensor. Furthermore, the layout of the framework structure needs to be adjusted via macroscale optimization to maintain the prescribed stiffness. Nevertheless, overly low objective elastic properties in microscale optimization might generate small-size struts, which increase the risk of high stress concentration under physiological loading conditions. In addition, the Boolean union operation between the porous structure and framework might generate different global structures of the porous cage due to different relative positions in operation. The porous cage can maintain its overall stiffness; however, thin-walled structures should be avoided in order to reduce the risk of local collapse. Based on the present approach, a porous structure with high stiffness can be obtained via microscale optimization and used to substitute the framework to construct the functional graded porous cage. To maintain the overall stiffness, macroscale optimization also needs to be reconducted to determine the layout of unit cells with different stiffnesses. Moreover, the proposed approach can be extended to design cages with other shapes or materials and additional types of orthopedic implants.

Despite the consensus that the elimination of stiffness discrepancy between implants and adjacent bones contributes to reducing stress shielding, the optimum stiffness of the cage for fusion remains undefined. The cage designed in the current study possesses a similar stiffness to adjacent bone endplates and exhibits satisfactory biomechanical performance in the numerical simulation. Unit cells with anisotropic mechanical properties or a porous cage with other stiffness values can also be obtained using the proposed approach through further research regarding the complex mechanical requirements of the fusion cage.

There are certain limitations of this study. Due to the requirement of cell ingrowth and constraint of fabricating precision, a unit cell with 1 mm length is adopted in microscale optimization. The periodic boundary is unfeasible for calculating the effective elasticity tensor of finitely repeated unit cells; however, the porous cage primarily resists compression loads in the vertical direction under physiological loading conditions. More than 6 unit cells are repeated along the main loading direction of porous cage, which confirms the feasibility of adopting the effective elasticity modulus in the literature [57]. Moreover, the detailed meshed porous cage is used to assess the stress distribution on bone endplates and the cage. The solid-mimic porous cage, which is used to evaluate the SED of bone grafts, exhibits comparable stiffness to the porous cage under physiological loading conditions. The stage after complete arthrodesis and bone growth into the porous cage is not considered in this study. To improve the calculation efficiency, muscles around the lumbar spine, an important tissue maintaining the stability of the lumbar spine, are not included in the FEM model. Most tissues of the lumbar spine are assumed as linear elastic materials in the simulation, which may affect the precision of results. Nonetheless, the trend of predicted results could not be affected. The numerical simulation demonstrates the biomechanical performance of the designed porous cage under specified loading conditions, while the evaluation of real-world performance of the porous cage warrants further experiments and clinical studies.

Conclusions

This study presents a multiscale topology optimization approach for designing a porous fusion cage with prescribed stiffness, including microscale optimization to obtain the unit cell with specified elastic properties and macroscale optimization to determine the layout of the framework structure over the porous cage. From a biomechanical point of view, the numerical simulation of TLIF verifies that the designed porous cage can reduce the risk of stress shielding and cage subsidence. The solid-mimic porous cage enables the prediction of stress distribution on bone endplates and frameworks of the porous cage, but fails to predict the peak stress on the porous structure. Thin-walled structures should be avoided in porous cage development to reduce the risk of local stress concentration. In addition, the morphological

and mechanical discrepancies between as-designed and fabricated structures measured by SLM indicate the necessity of further research on the optimization of fabricating parameters and post-treatments. The present multiscale optimization approach can be extended to the development of cages with other shapes or materials, as well as additional types of orthopedic implants.

Acknowledgements This work was financially supported by the National Natural Science Foundation of China (No. 51975336), the Key Basic Research Project of Natural Science Foundation of Shandong Province, China (No. ZR2018ZB0106), and the Key Research and Development Program of Shandong Province, China (No. 2019JZZY010112).

Author contributions HW contributed to conceptualization, methodology, software, and writing—original draft; YW contributed to supervision, writing—review, editing, and funding acquisition; QL contributed to software, formal analysis, and writing—review; XL contributed to resources, formal analysis, and writing–review; MY, XZ, and QS contributed to formal analysis and data curation; YX contributed to software and writing—review; ZL contributed to supervision and writing—review.

Declarations

Conflict of interest The authors declare that there is no conflict of interest.

Ethical approval This study does not contain any studies with human or animal subjects performed by any of the authors.

References

1. Nemoto O, Asazuma T, Yato Y et al (2014) Comparison of fusion rates following transforaminal lumbar interbody fusion using polyetheretherketone cages or titanium cages with transpedicular instrumentation. Eur Spine J 23:2150–2155. https://doi.org/10.1007/s00586-014-3466-9
2. Tan XP, Tan YJ, Chow CSL et al (2017) Metallic powder-bed based 3D printing of cellular scaffolds for orthopaedic implants: a state-of-the-art review on manufacturing, topological design, mechanical properties and biocompatibility. Mater Sci Eng C 76:1328–1343. https://doi.org/10.1016/j.msec.2017.02.094
3. Caparrós C, Guillem-Martí J, Molmeneu M et al (2014) Mechanical properties and in vitro biological response to porous titanium alloys prepared for use in intervertebral implants. J Mech Behav Biomed Mater 39:79–86. https://doi.org/10.1016/j.jmbbm.2014.05.029
4. Chen Y, Wang X, Lu X et al (2013) Comparison of titanium and polyetheretherketone (PEEK) cages in the surgical treatment of multilevel cervical spondylotic myelopathy: a prospective, randomized, control study with over 7-year follow-up. Eur Spine J 22:1539–1546. https://doi.org/10.1007/s00586-013-2772-y
5. van Dijk M, Smit TH, Sugihara S et al (2002) The effect of cage stiffness on the rate of lumbar interbody fusion. Spine (Phila Pa 1976) 27:682–688. https://doi.org/10.1097/00007632-200204010-00003
6. Mobbs RJ, Phan K, Assem Y et al (2016) Combination Ti/PEEK ALIF cage for anterior lumbar interbody fusion: early clinical and radiological results. J Clin Neurosci 34:94–99. https://doi.org/10.1016/j.jocn.2016.05.028
7. Lee YH, Chung CJ, Wang CW et al (2016) Computational comparison of three posterior lumbar interbody fusion techniques by using porous titanium interbody cages with 50% porosity. Comput Biol Med 71:35–45. https://doi.org/10.1016/j.compbiomed.2016.01.024
8. Chatham LS, Patel VV, Yakacki CM et al (2017) Interbody spacer material properties and design conformity for reducing subsidence during lumbar interbody fusion. J Biomech Eng 139:051005. https://doi.org/10.1115/1.4036312
9. Sato T, Yonezawa I, Todo M et al (2018) Biomechanical effects of implant materials on posterior lumbar interbody fusion: comparison of polyetheretherketone and titanium spacers using finite element analysis and considering bone density. J Biomed Sci Eng 11:45–59. https://doi.org/10.4236/jbise.2018.114005
10. Kurtz SM, Devine JN, Olivares-Navarrete R et al (2012) PEEK biomaterials in trauma, orthopedic, and spinal implants. Biomaterials 12:4845–4869. https://doi.org/10.1016/J.SPINEE.2012.02.002
11. Lowther M, Louth S, Davey A et al (2019) Clinical, industrial, and research perspectives on powder bed fusion additively manufactured metal implants. Addit Manuf 28:565–584. https://doi.org/10.1016/j.addma.2019.05.033
12. du Plessis A, Broeckhoven C, Yadroitsava I et al (2019) Beautiful and functional: a review of biomimetic design in additive manufacturing. Addit Manuf 27:408–427. https://doi.org/10.1016/j.addma.2019.03.033
13. Lee DY, Park YJ, Song SY et al (2018) Risk factors for posterior cage migration after lumbar interbody fusion surgery. Asian Spine J 12:59–68. https://doi.org/10.4184/asj.2018.12.1.59
14. Zhang Z, Li H, Fogel GR et al (2018) Biomechanical analysis of porous additive manufactured cages for lateral lumbar interbody fusion: a finite element analysis. World Neurosurg 111:e581–e591. https://doi.org/10.1016/j.wneu.2017.12.127
15. McGilvray KC, Easley J, Seim HB et al (2018) Bony ingrowth potential of 3D-printed porous titanium alloy: a direct comparison of interbody cage materials in an in vivo ovine lumbar fusion model. Spine J 18:1250–1260. https://doi.org/10.1016/j.spinee.2018.02.018
16. Chen C, Hao Y, Bai X et al (2019) 3D printed porous Ti6Al4V cage: effects of additive angle on surface properties and biocompatibility; bone ingrowth in Beagle tibia model. Mater Des 175:107824. https://doi.org/10.1016/j.matdes.2019.107824
17. Li P, Jiang W, Yan J et al (2019) A novel 3D printed cage with microporous structure and in vivo fusion function. J Biomed Mater Res Part A 107:1386–1392. https://doi.org/10.1002/jbm.a.36652
18. Wang X, Xu S, Zhou S et al (2016) Topological design and additive manufacturing of porous metals for bone scaffolds and orthopaedic implants: a review. Biomaterials 83:127–141. https://doi.org/10.1016/j.biomaterials.2016.01.012
19. Al-Ketan O, Rowshan R, Abu Al-Rub RK (2018) Topology-mechanical property relationship of 3D printed strut, skeletal, and sheet based periodic metallic cellular materials. Addit Manuf 19:167–183. https://doi.org/10.1016/j.addma.2017.12.006
20. Zhang A, Chen H, Liu Y et al (2021) Customized reconstructive prosthesis design based on topological optimization to treat severe proximal tibia defect. Bio-Des Manuf 4:87–99. https://doi.org/10.1007/s42242-020-00102-7
21. Cai Z, Liu Z, Hu X et al (2019) The effect of porosity on the mechanical properties of 3D-printed triply periodic minimal surface (TPMS) bioscaffold. Bio-Des Manuf 2:242–255. https://doi.org/10.1007/s42242-019-00054-7
22. Chen Y, Schellekens M, Zhou S et al (2011) Design optimization of scaffold microstructures using wall shear stress

criterion towards regulated flow-induced erosion. J Biomech Eng 133:081008. https://doi.org/10.1115/1.4004918
23. Xiao DM, Yang YQ, Su XB et al (2012) Topology optimization of microstructure and selective laser melting fabrication for metallic biomaterial scaffolds. Trans Nonferrous Met Soc China 22:2554–2561. https://doi.org/10.1016/S1003-6326(11)61500-8
24. Almeida HA, Bártolo PJ (2013) Topological optimisation of scaffolds for tissue engineering. Procedia Eng 59:298–306. https://doi.org/10.1016/j.proeng.2013.05.125
25. Xiao D, Yang Y, Su X et al (2013) An integrated approach of topology optimized design and selective laser melting process for titanium implants materials. Biomed Mater Eng 23:433–445. https://doi.org/10.3233/BME-130765
26. Yang XY, Huang X, Rong JH et al (2013) Design of 3D orthotropic materials with prescribed ratios for effective Young's moduli. Comput Mater Sci 67:229–237. https://doi.org/10.1016/j.commatsci.2012.08.043
27. Guest JK, Prévost JH (2006) Optimizing multifunctional materials: design of microstructures for maximized stiffness and fluid permeability. Int J Solids Struct 43:7028–7047. https://doi.org/10.1016/j.ijsolstr.2006.03.001
28. Moussa A, Tanzer M, Pasini D (2018) Cervical fusion cage computationally optimized with porous architected titanium for minimized subsidence. J Mech Behav Biomed Mater 85:134–151. https://doi.org/10.1016/j.jmbbm.2018.05.040
29. Wang H, Wan Y, Li Q et al (2020) Porous fusion cage design via integrated global-local topology optimization and biomechanical analysis of performance. J Mech Behav Biomed Mater 112:103982. https://doi.org/10.1016/j.jmbbm.2020.103982
30. Hassani B, Hinton E (1998) A review of homogenization and topology optimization II—analytical and numerical solution of homogenization equations. Comput Struct 69:719–738. https://doi.org/10.1016/S0045-7949(98)00132-1
31. Hassani B, Hinton E (1998) A review of homogenization and topology optimization I—Homogenization theory for media with periodic structure. Comput Struct 69:707–717. https://doi.org/10.1016/S0045-7949(98)00131-X
32. Hassani B, Hinton E (1998) A review of homogenization and topology optimization III—topology optimization using optimality criteria. Comput Struct 69:739–756. https://doi.org/10.1016/S0045-7949(98)00133-3
33. Arabnejad S, Burnett Johnston R, Pura JA et al (2016) High-strength porous biomaterials for bone replacement: a strategy to assess the interplay between cell morphology, mechanical properties, bone ingrowth and manufacturing constraints. Acta Biomater 30:345–356. https://doi.org/10.1016/j.actbio.2015.10.048
34. Svanberg K (1987) The method of moving asymptotes—a new method for structural optimization. Int J Numer Methods Eng 24:359–373. https://doi.org/10.1002/nme.1620240207
35. Provaggi E, Capelli C, Rahmani B et al (2019) 3D printing assisted finite element analysis for optimising the manufacturing parameters of a lumbar fusion cage. Mater Des 163:107540. https://doi.org/10.1016/j.matdes.2018.107540
36. Wang H, Wan Y, Liu X et al (2020) Biomechanical analysis of combination Ti/PEEK fusion cage designed with topology optimization. Int J Appl Electromagn Mech 1:1–8. https://doi.org/10.3233/jae-209442
37. Polikeit A, Ferguson SJ, Nolte LP et al (2003) Factors influencing stresses in the lumbar spine after the insertion of intervertebral cages: finite element analysis. Eur Spine J 12:413–420. https://doi.org/10.1007/s00586-002-0505-8
38. Kim K, Park WM, Kim YH et al (2010) Stress analysis in a pedicle screw fixation system with flexible rods in the lumbar spine. Proc Inst Mech Eng Part H J Eng Med 224:477–485. https://doi.org/10.1243/09544119JEIM611
39. Goel VK, Mehta A, Jangra J et al (2007) Anatomic facet replacement system (AFRS) restoration of lumbar segment mechanics to intact: a finite element study and in vitro cadaver investigation. Int J Spine Surg 1:46–54. https://doi.org/10.1016/sasj-2006-0010-rr
40. Lin CY, Hsiao CC, Chen PQ et al (2004) Interbody fusion cage design using integrated global layout and local microstructure topology optimization. Spine (Phila Pa 1976) 29:1747–1754. https://doi.org/10.1097/01.BRS.0000134573.14150.1A
41. Eidel B, Gote A, Fritzen CP et al (2019) Tibial implant fixation in TKA worth a revision?—to avoid stress-shielding even for stiff metallic implants. Comput Method Biomech 24:320–332. https://doi.org/10.1080/10255842.2020.1830274
42. Zhang QH, Cossey A, Tong J (2016) Stress shielding in periprosthetic bone following a total knee replacement: effects of implant material, design and alignment. Med Eng Phys 38:1481–1488. https://doi.org/10.1016/j.medengphy.2016.09.018
43. Kim Y (2001) Prediction of mechanical behaviors at interfaces between bone and two interbody cages of lumbar spine segments. Spine (Phila Pa 1976) 26:1437–1442. https://doi.org/10.1097/00007632-200107010-00010
44. Kim DH, Jeong ST, Lee SS (2009) Posterior lumbar interbody fusion using a unilateral single cage and a local morselized bone graft in the degenerative lumbar spine. Clin Orthop Surg 1:214–221. https://doi.org/10.4055/cios.2009.1.4.214
45. Yang L, Yan C, Cao W et al (2019) Compression–compression fatigue behaviour of gyroid-type triply periodic minimal surface porous structures fabricated by selective laser melting. Acta Mater 181:49–66. https://doi.org/10.1016/j.actamat.2019.09.042
46. Simon JL, Michna S, Lewis JA et al (2007) In vivo bone response to 3D periodic hydroxyapatite scaffolds assembled by direct ink writing. J Biomed Mater Res Part A 83A:747–758. https://doi.org/10.1002/jbm.a.31329
47. Murphy CM, Haugh MG, O'Brien FJ (2010) The effect of mean pore size on cell attachment, proliferation and migration in collagen-glycosaminoglycan scaffolds for bone tissue engineering. Biomaterials 31:461–466. https://doi.org/10.1016/j.biomaterials.2009.09.063
48. Ran Q, Yang W, Hu Y et al (2018) Osteogenesis of 3D printed porous Ti6Al4V implants with different pore sizes. J Mech Behav Biomed Mater 84:1–11. https://doi.org/10.1016/j.jmbbm.2018.04.010
49. Perez RA, Mestres G (2016) Role of pore size and morphology in musculo-skeletal tissue regeneration. Mater Sci Eng C 61:922–939. https://doi.org/10.1016/j.msec.2015.12.087
50. Zhang Z, Li H, Fogel GR et al (2018) Finite element model predicts the biomechanical performance of transforaminal lumbar interbody fusion with various porous additive manufactured cages. Comput Biol Med 95:167–174. https://doi.org/10.1016/j.compbiomed.2018.02.016
51. Adam C, Pearcy M, McCombe P (2003) Stress analysis of interbody fusion—finite element modelling of intervertebral implant and vertebral body. Clin Biomech 18:265–272. https://doi.org/10.1016/S0268-0033(03)00022-6
52. Cabraja M, Oezdemir S, Koeppen D et al (2012) Anterior cervical discectomy and fusion: comparison of titanium and polyetheretherketone cages. BMC Musculoskelet Disord 13:172. https://doi.org/10.1186/1471-2474-13-172
53. Simoneau C, Terriault P, Jetté B et al (2017) Development of a porous metallic femoral stem: design, manufacturing, simulation and mechanical testing. Mater Des 114:546–556. https://doi.org/10.1016/j.matdes.2016.10.064
54. Sallica-Leva E, Jardini AL, Fogagnolo JB (2013) Microstructure and mechanical behavior of porous Ti–6Al–4V parts obtained by selective laser melting. J Mech Behav Biomed Mater 26:98–108. https://doi.org/10.1016/j.jmbbm.2013.05.011

55. Wauthle R, Vrancken B, Beynaerts B et al (2015) Effects of build orientation and heat treatment on the microstructure and mechanical properties of selective laser melted Ti6Al4V lattice structures. Addit Manuf 5:77–84. https://doi.org/10.1016/j.addma.2014.12.008
56. Campoli G, Borleffs MS, Amin Yavari S et al (2013) Mechanical properties of open-cell metallic biomaterials manufactured using additive manufacturing. Mater Des 49:957–965. https://doi.org/10.1016/j.matdes.2013.01.071
57. Coelho PG, Hollister SJ, Flanagan CL et al (2015) Bioresorbable scaffolds for bone tissue engineering: optimal design, fabrication, mechanical testing and scale-size effects analysis. Med Eng Phys 37:287–296. https://doi.org/10.1016/j.medengphy.2015.01.004